

sense that it transforms from a nonmagnetic insulating phase to a magnetic metallic phase under applied pressures on the order of 10 GPa (42–45), which is in contrast to other metallic rare earth hexaborides in which the f -electrons order magnetically in the ambient ground state. Our observation of a large three-dimensional conduction electron Fermi surface revealed by quantum oscillations may be related to reports of a residual density of states at the Fermi energy in SmB_6 through measurements of heat capacity (23, 46), optical conductivity (47), Raman scattering (48), and neutron scattering (49). Another possibility is that quantum oscillations could arise even in a system with a gap in the excitation spectrum at the Fermi energy, provided that the size of the gap is not much larger than the cyclotron energy (50). Within this scenario, the residual density of states observed at the Fermi energy with complementary measurements and the steep upturn in quantum oscillation amplitude we observe at low temperatures appear challenging to explain.

REFERENCES AND NOTES

- A. C. Hewson, *The Kondo Problem to Heavy Fermions* (Cambridge Univ. Press, Cambridge, 1997).
- N. F. Mott, *Philos. Mag.* **30**, 403–416 (1974).
- G. Aeppli, Z. Fisk, *Comments Condens. Matt. Phys.* **16**, 155 (1992).
- A. J. Schofield, *Contemp. Phys.* **40**, 95–115 (1999).
- J. E. Moore, *Nature* **464**, 194–198 (2010).
- S. Paschen et al., *Nature* **432**, 881–885 (2004).
- S. A. Grigera et al., *Science* **306**, 1154–1157 (2004).
- F. Lévy, I. Sheikin, B. Grenier, A. D. Huxley, *Science* **309**, 1343–1346 (2005).
- C. Pfleiderer, S. R. Julian, G. G. Lonzarich, *Nature* **414**, 427–430 (2001).
- N. D. Mathur et al., *Nature* **394**, 39–43 (1998).
- H. Hegger et al., *Phys. Rev. Lett.* **84**, 4986–4989 (2000).
- H. Löhneysen et al., *Phys. Rev. Lett.* **72**, 3262–3265 (1994).
- J. Flouquet, *Prog. Low Temp. Phys.* **15**, 139–281 (2005).
- C. M. Varma, Z. Nussinov, W. van Saarloos, *Phys. Rep.* **361**, 267–417 (2002).
- A. Menth, E. Buehler, T. H. Geballe, *Phys. Rev. Lett.* **22**, 295–297 (1969).
- S. Behler, K. Winzer, *Z. Phys. B Condens. Matter* **82**, 355–361 (1991).
- Y. Ōnuki, T. Komatsubara, P. H. P. Reinders, M. Springford, *J. Phys. Soc. Jpn.* **58**, 3698 (1989).
- D. Shoenberg, *Magnetic Oscillations in Metals* (Cambridge Univ. Press, Cambridge, 1984).
- M. Ciomaga Hatnean, M. R. Lees, D. M. K. Paul, G. Balakrishnan, *Sci. Rep.* **3**, 3071 (2013).
- J. Morillo, C.-H. de Novion, J. Jun, *Solid State Commun.* **48**, 315–319 (1983).
- G. Priztáš, S. Gabáni, K. Flachbart, V. Filipov, N. Shitsevalova, *JPS Conf. Proc.* **3**, 012021 (2014).
- G. Li et al., *Science* **346**, 1208–1212 (2014).
- Materials and methods are available as supplementary materials on Science Online.
- M. Dzero, K. Sun, V. Galitski, P. Coleman, *Phys. Rev. Lett.* **104**, 106408 (2010).
- M. Aono et al., *Surf. Sci.* **86**, 631–637 (1979).
- S. E. Sebastian, N. Harrison, G. G. Lonzarich, *Rep. Prog. Phys.* **75**, 102501 (2012).
- L. Taillefer, G. G. Lonzarich, *Phys. Rev. Lett.* **60**, 1570–1573 (1988).
- P. H. P. Reinders, M. Springford, P. T. Coleridge, R. Boulet, D. Ravot, *Phys. Rev. Lett.* **57**, 1631–1634 (1986).
- H. Shishido, R. Settai, H. Harima, Y. Onuki, *J. Phys. Soc. Jpn.* **74**, 1103–1106 (2005).
- D. C. Tsui, H. L. Stormer, A. C. Gossard, *Phys. Rev. Lett.* **48**, 1559–1562 (1982).
- R. B. Laughlin, *Phys. Rev. Lett.* **50**, 1395–1398 (1983).
- M. Elliott, T. Ellis, M. Springford, *J. Phys. F Met. Phys.* **10**, 2681–2706 (1980).
- A. McCollam, J.-S. Xia, J. Flouquet, D. Aoki, S. R. Julian, *Physica B* **403**, 717–720 (2008).
- P. K. Biswas et al., *Phys. Rev. B* **89**, 161107 (2014).
- R. L. Cohen, M. Eibschütz, K. W. West, *Phys. Rev. Lett.* **24**, 383–386 (1970).
- P. Coleman, E. Miranda, A. Tsvetlik, *Physica B* **186**, 362–364 (1993).
- H. Kleinert, *Gauge Fields in Condensed Matter* (World Scientific, Singapore, 1988).
- T. Kasuya, *J. Phys. Soc. Jpn.* **63**, 397–400 (1994).
- Q. Si, S. Paschen, *Phys. Status Solidi B* **250**, 425–438 (2013).
- M. Mizumaki, S. Tsutsui, F. Iga, *J. Phys. Conf. Ser.* **176**, 012034 (2009).
- Y. Matsumoto et al., *Science* **331**, 316–319 (2011).
- J. C. Cooley, M. C. Aronson, Z. Fisk, P. C. Canfield, *Phys. Rev. Lett.* **74**, 1629–1632 (1995).
- A. Barla et al., *Phys. Rev. Lett.* **94**, 166401 (2005).
- J. Derr et al., *J. Phys. Condens. Matter* **18**, 2089–2106 (2006).
- J. Derr et al., *Phys. Rev. B* **77**, 193107 (2008).
- K. Flachbart et al., *Physica B* **378**, 610–611 (2006).
- T. Namba et al., *Physica B* **186**, 440–443 (1993).
- P. Nyhus, S. L. Cooper, Z. Fisk, J. Sarrao, *Phys. Rev. B* **52**, R14308–R14311 (1995).
- P. A. Alekseev, J.-M. Mignot, J. Rossat-Mignod, V. N. Lazukov, I. P. Sadikov, *Physica B* **186**, 384–386 (1993).
- K. Miyake, *Physica B* **186**, 115–117 (1993).

ACKNOWLEDGMENTS

B.S.T., Y.-T.H., M.H., M.K., A.S., and S.E.S. acknowledge support from the Royal Society, the Winton Programme for the Physics of Sustainability, and the European Research Council (ERC) under the European Union's Seventh Framework Programme (grant FP/2007-2013)/ERC Grant Agreement 337425. B.Z. and L.B. acknowledge support from the U.S. Department of Energy (DOE)–Basic Energy Sciences (BES) through award DE-SC0002613. M.C.H. and G.B. acknowledge support from Engineering and Physical

Sciences Research Council (EPSRC) grant EP/L014963/1. N.H. and Z.Z. acknowledge support from the DOE Office of Science, BES–Materials Science and Engineering “Science of 100 Tesla” program. M.D.J. acknowledges support for this project by the Office of Naval Research (ONR) through the Naval Research Laboratory’s Basic Research Program. G.G.L. acknowledges support from EPSRC grant EP/K012894/1. A portion of this work was performed at the National High Magnetic Field Laboratory, which is supported by NSF Cooperative Agreement DMR-1157490 and the state of Florida. We acknowledge valuable inputs from G. Baskaran, D. Benkert, A. K. Cheetham, D. Chowdhury, P. Coleman, N. R. Cooper, M. P. M. Dean, O. Ertem, J. Flouquet, R. H. Friend, R. Golombok, C. Harris, S. A. Hartnoll, T. Kasuya, G. Khalullin, E.-A. Kim, J. Knolle, P. A. Lee, P. B. Littlewood, C. Liu, K. Miyake, J. E. Moore, O. Petrenko, S. Sachdev, A. Shekhter, N. Shitsevalova, Q. Si, A. Thomson, S. Todadri, C. M. Varma, and J. Zaanen. We thank magnet laboratory personnel, including J. Billings, R. Carrier, E. S. Choi, B. L. Dalton, D. Freeman, L. J. Gordon, M. Hicks, C. H. Mielke, J. M. Petty, and J. N. Piotrowski, for their assistance. Data will be made available at the institutional data repository www.data.cam.ac.uk/data-repository.

SUPPLEMENTARY MATERIALS

www.sciencemag.org/content/349/6245/287/suppl/DC1
Materials and Methods
Supplementary Text
Figs. S1 to S5
Table S1
References (51–57)

28 January 2015; accepted 24 June 2015
Published online 2 July 2015
10.1126/science.aaa7974

NANOPARTICLE IMAGING

3D structure of individual nanocrystals in solution by electron microscopy

Jungwon Park,^{1,2,3*} Hans Elmlund,^{4,5*} Peter Ercius,^{6*} Jong Min Yuk,^{7,8,9} David T. Limmer,¹⁰ Qian Chen,^{1,8,11} Kwanpyo Kim,¹² Sang Hoon Han,¹³ David A. Weitz,^{2,3} A. Zettl,^{7,8,9} A. Paul Alivisatos^{1,8,9,†}

Knowledge about the synthesis, growth mechanisms, and physical properties of colloidal nanoparticles has been limited by technical impediments. We introduce a method for determining three-dimensional (3D) structures of individual nanoparticles in solution. We combine a graphene liquid cell, high-resolution transmission electron microscopy, a direct electron detector, and an algorithm for single-particle 3D reconstruction originally developed for analysis of biological molecules. This method yielded two 3D structures of individual platinum nanocrystals at near-atomic resolution. Because our method derives the 3D structure from images of individual nanoparticles rotating freely in solution, it enables the analysis of heterogeneous populations of potentially unordered nanoparticles that are synthesized in solution, thereby providing a means to understand the structure and stability of defects at the nanoscale.

Colloidal nanoparticles are clusters of hundreds to thousands of inorganic atoms typically surrounded by organic ligands that stabilize them in solution. The atomic arrangement of colloidal nanoparticles determines their chemical and physical properties, which are distinct from bulk materials and can be exploited for many applications in biological imaging, renewable energy, catalysis, and more. The 3D atomic arrangement on the surface and in the core of a nanocrystal influences the electronic struc-

ture, which affects how the nanocrystal functions in catalysis or how it interacts with other components at the atomic scale (1). Introduction of atomic dopants, surface adatoms, defects, and grain boundaries alters the chemical properties of nanocrystals (2). Ensembles of synthesized nanocrystals in solution are structurally inhomogeneous because of the stochastic nature of nanocrystal nucleation and growth (3, 4). Therefore, a method for determination of the 3D atomic arrangement of individual unique nanoparticles in solution is needed.

Electron tomography is routinely used for 3D analysis of materials (5–9). This method cannot be applied to individual particles in a liquid because it relies on acquisition of images of a single object at many different tilt angles over a period of 2 to 5 hours, assuming the object is static during the entire acquisition. Single-particle cryo-electron microscopy (cryo-EM) is a common method for the determination of 3D structures in biological sciences. The average 3D Coulomb potential map (i.e., density) of a protein is reconstructed from tens of thousands of transmission electron microscopy (TEM) images of randomly oriented copies of the same protein embedded in vitreous ice (10). The unknown 3D projection angles of the images are determined by computational methods (11). Single-particle cryo-EM has succeeded in reconstructing biological molecules with nearly 3 Å resolution (10, 12). A similar approach was recently applied to reconstruct the atomic structure of homogeneous ultrasmall gold clusters (13). However, the single-particle method is not readily applicable to 3D reconstruction of colloidal nanoparticles because of their intrinsic structural inhomogeneity at the atomic level.

TEM has undergone technical improvements in the past decades (5, 14–17). The image resolution has been improved with the introduction of electron lens aberration correctors (15). The development of direct electron detectors has led to improvements in image quality and rapid acquisition of movies that allow for compensation for beam-induced specimen motion, thereby providing a substantial enhancement to single-particle cryo-EM (18).

We present a hybrid method for reconstructing the 3D structures of individual nanoparticles in solution. The method represents a combination of three technological advancements from TEM imaging in biological and materials science: (i) the development of graphene as a covering to hold a liquid in vacuum (the so-called graphene liquid cell, or GLC) that allows atomic-resolution imaging of nanoparticles that move and rotate freely in solution by aberration-corrected TEM (3, 19); (ii) the advent of direct electron detectors, producing movies with millisecond

frame-to-frame time resolution of the rotating nanocrystals (18); and (iii) a theory for ab initio single-particle 3D reconstruction, used to solve the inverse problem of recovering the unknown 3D orientations of the individual noisy nanocrystal projections (11). The resulting hybrid technique, 3D structure identification of nanoparticles by GLC EM (abbreviated as SINGLE), was used to separately reconstruct the 3D structures of two individual Pt nanocrystals in solution.

Pt nanoparticles were chosen because of their high electron scattering strength, because their detailed atomic structure is important for catalysis, and because earlier graphene liquid cell studies have shown that they grow by nanoparticle aggregation, resulting in complex structures that are not possible to determine by any previously developed method. Pt nanocrystals with sub-2 nm diameter were prepared in solution. Two graphene sheets were grown by the chemical vapor deposition method and used to entrap solvated nanocrystals (3). The graphene provides an ultrathin covering of material to maintain liquid conditions in the TEM vacuum and presents an inert surface onto which the nanoparticles do not adsorb. The translational and rotational motions of the particles in liquid pockets with sub-50 nm diameter were imaged in situ using TEAM I, a TEM instrument

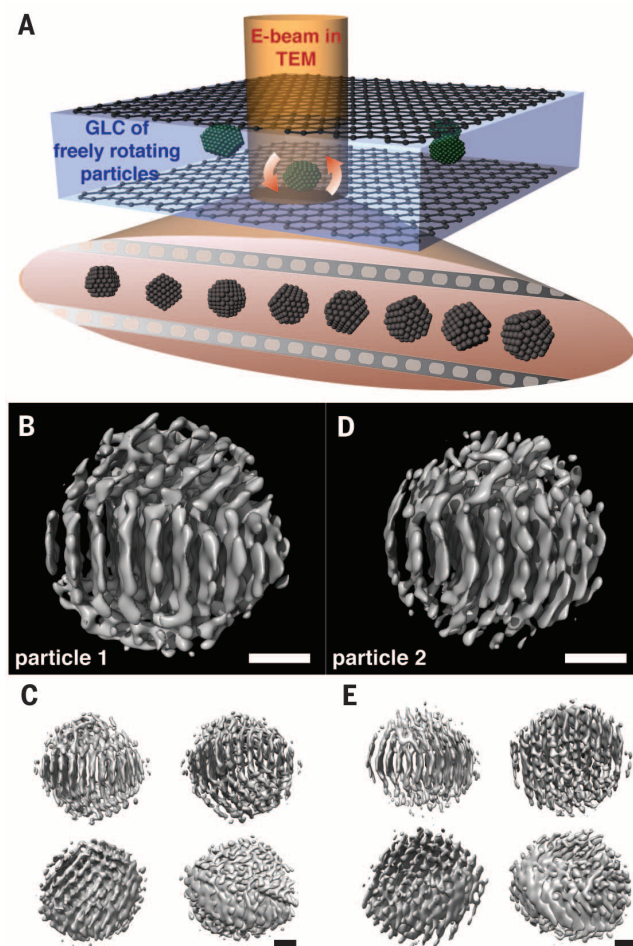
with geometrical and chromatic aberration correction, operated at 300 kV using a direct electron detector (Fig. 1A). The corrector was set to apply a slightly negative spherical aberration coefficient of about $-10\ \mu\text{m}$. Under these imaging conditions, we produced white atom contrast when using a small underfocus value of 30 to 50 Å.

Movies of the moving particles had a temporal resolution of 50 frames/s, a field of view of 1024×1024 pixels, and a Nyquist sampling limit of 0.56 Å. Each movie frame represents a 2D projection of many particles in random orientations. To reconstruct the individual 3D structures, we chose a small region around each single particle of interest in each individual frame to create a set of projections per particle. The 3D orientations of the resulting series of noisy 2D images of a single rotating particle were recovered computationally using an ab initio 3D reconstruction algorithm adapted from one originally developed to recover orientations from cryo-EM images of many identical individual particles (11).

Although the TEM movies contain many particles, not all particles could be used for reconstruction because of overlap with other particles and insufficient rotation. Here, we present the two most reliable 3D reconstructions from a 1561-image series (particle 1 in Fig. 1, B and C, and movie S1) and a 1171-image series (particle 2

Fig. 1. Schematic illustration of in situ TEM imaging of Pt nanocrystals freely rotating in a graphene liquid cell (GLC) and 3D EM density maps calculated from individual Pt nanoparticles in solution.

(A) A movie of the single rotating Pt nanocrystal provides 2D projected TEM still snapshots in many orientations for ab initio particle reconstruction. (B) EM density map obtained from the 3D reconstruction of particle 1. The orientation of the particle is aligned to expose {111} planes of the core domain. Three distinct crystal domains can be identified. (C) 3D EM density map of particle 1 with alternative viewing angles. (D) EM density map obtained from the 3D reconstruction of particle 2. (E) 3D EM density map of particle 2 with alternative viewing angles. Each panel in (C) and (E) presents the two particles with the same angle and direction with respect to the orientations in (B) and (D). Scale bars, 0.5 nm.



¹Department of Chemistry, University of California, Berkeley, CA 94720, USA. ²Department of Applied Physics, Harvard University, Cambridge, MA 02138, USA. ³School of Engineering and Applied Sciences, Harvard University, Cambridge, MA 02138, USA. ⁴Department of Biochemistry and Molecular Biology, School of Biomedical Sciences, Monash University, Clayton, VIC 3800, Australia. ⁵ARC Centre of Excellence for Advanced Molecular Imaging, Clayton, VIC 3800, Australia. ⁶Molecular Foundry, Lawrence Berkeley National Laboratory, Berkeley, CA 94720, USA. ⁷Department of Physics, University of California, Berkeley, CA 94720, USA. ⁸Materials Sciences Division, Lawrence Berkeley National Laboratory, Berkeley, CA 94720, USA. ⁹Kavli Energy NanoScience Institute, Berkeley, CA 94720, USA. ¹⁰Princeton Center for Theoretical Science, Princeton University, Princeton, NJ 08540, USA. ¹¹Miller Institute for Basic Research in Science, University of California, Berkeley, CA 93720, USA. ¹²Department of Physics, Ulsan National Institute of Science and Technology, Ulsan 689-798, South Korea. ¹³Amore-Pacific Co. R&D Center, Yongin 446-829, South Korea.

*These authors contributed equally to this work. †Corresponding author. E-mail: alivis@berkeley.edu

in Fig. 1, D and E, and movie S2). Shown in Fig. 1, B to E, are the EM density maps of the two Pt nanocrystals. The rendered particle volumes are 5300 \AA^3 (diameter 22 \AA) for particle 1 and 4800 \AA^3 (diameter 20 \AA) for particle 2. Along with the direct visualization of the spatial distribution of

Pt atomic planes, external and internal structures of the particle are uncovered. Each reconstruction shows three distinct crystal domains in both of the Pt particles. In Fig. 1, B and D, we show views of the EM maps in an orientation that reveals distinct lattice planes of the core domain.

Differently oriented 3D density maps are shown in Fig. 1, C and E, and movies S1 and S2.

Our 3D reconstruction methodology produced reconstructions at near-atomic resolution from relatively small sets of noisy experimental TEM images of nanocrystals in random orientations.

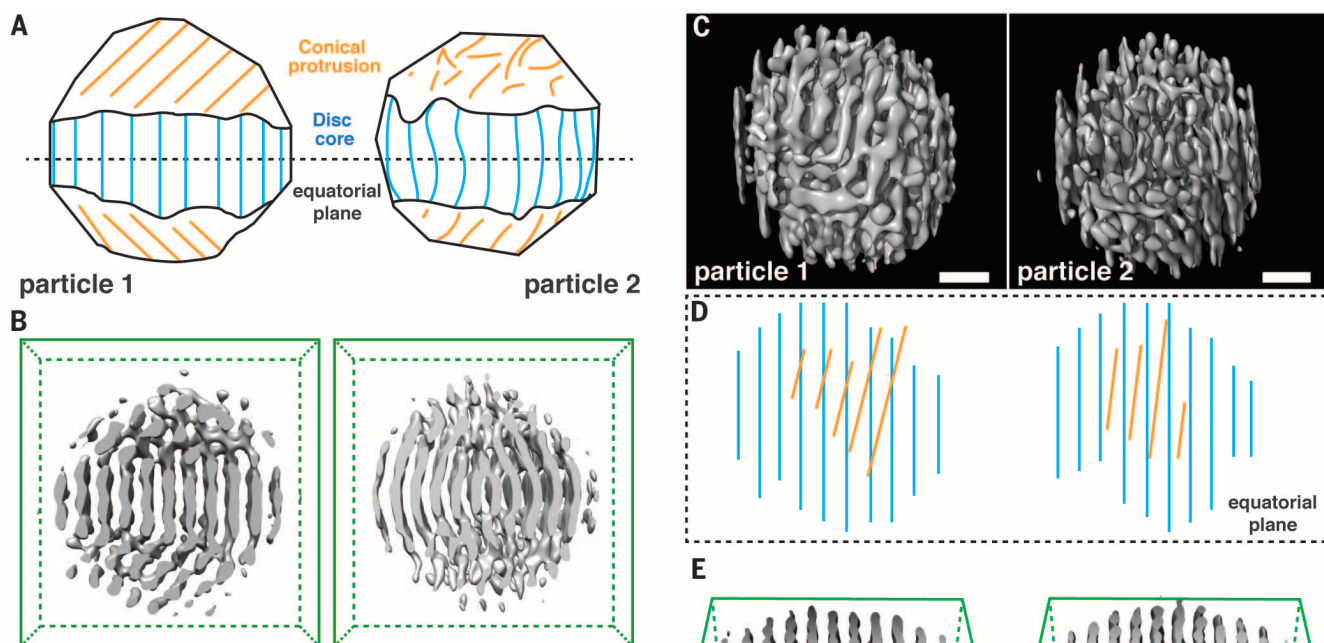
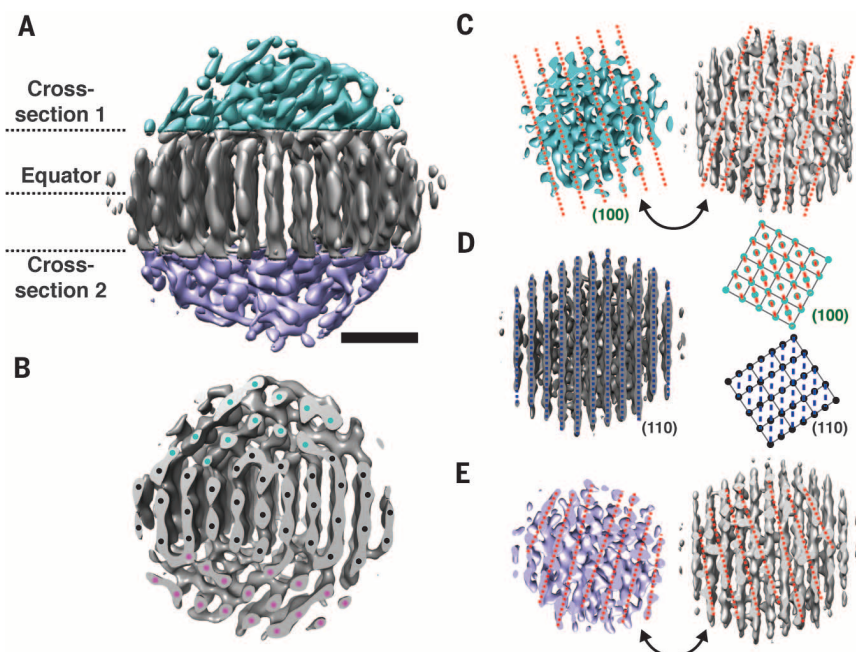


Fig. 2. The underlying structural principle of the small Pt nanoparticles studied here. (A) Schematic illustration of the front view of particles 1 and 2 shown in Fig. 1. Both particles are composed of a dense central disc of atomic planes (blue lines) with conical protrusions (orange lines) anchoring on each side of the disc. (B) Cross-sectional view of the EM density map of particle 1 and 2 along the vertical plane. (C) View orthogonal to (A), showing the overlaid lattices. Scale bars, 0.5 nm . (D) Schematic illustration of the top view of particles 1 and 2 shown in (C). (E) Cross-sectional view of the EM density map of particles 1 and 2 along the equatorial plane.

Fig. 3. Cross-sectional study of particle 1. (A) 3D density map of particle 1 with color coding to highlight the three sections. Cross sections 1 and 2 are in arbitrary positions near crystal domain interfaces. Scale bar, 0.5 nm . (B) Slab through the 3D reconstruction of particle 1 along the vertical plane, with tentative atomic positions indicated. ABC repeats of $\{111\}$ planes are visible. (C) Slab along cross section 1. The exposed (100) surface of the fcc Pt crystal is shown consistently in both exposed surfaces. Intersections with $\{111\}$ planes in the top domain are displayed by red dashed lines. (D) Slab along the equatorial plane of (A) exposes a (110) plane. The intersections with $\{111\}$ planes are shown by blue dashed lines. Pseudo-atomic structure (right) demonstrates the rotation angle (14°) between the (100) and (110) surfaces from the top and bottom domains, respectively. (E) Slab along cross section 2. The disordered (100) surface of the fcc Pt crystal is shown consistently in both exposed surfaces. Intersections with pseudo $\{111\}$ planes in the bottom domain are displayed by red dashed lines.



We tested the validity of SINGLE using 1000 multislice TEM simulations of a randomly oriented Pt nanocrystal with dodecahedral symmetry and corresponding size. Reconstructions were obtained from images with a signal-to-noise ratio (SNR) roughly corresponding to that of the experimental images (see fig. S1). This verified that the experimental images can conform to the projection-slice theorem with ideal microscope conditions (20).

To confirm the existence of a projected lattice in the experimental images, we calculated their power spectra, which showed distinct spots along different crystalline zone axes (fig. S2). Closer examination of the power spectra and corresponding orientation coverage throughout the image series revealed that each particle continuously undergoes small local rotations followed by rapid orientation changes, often accompanied by lateral movement. The noise variance in the individual frames of the movie exceeds the signal variance by approximately a factor of 5, despite the strong scattering from the heavy Pt atoms (movies S3 and S4 show 200 raw TEM images). Although sufficiently thin to observe atomic detail, the liquid between the graphene sheets introduces a

granular background, making it difficult to distinguish the facets of the nanocrystal in the individual frames. To enhance the image contrast and allow accurate 3D orientation determination, we averaged the image series in sets of five consecutive frames, resulting in a time resolution of ~100 ms. After frame averaging, we carefully scanned the image series to remove a small fraction (~20%) of those averages that did not show any lattice contrast because the particles had moved out of the narrow ideal focal plane of the aberration-corrected microscope.

Initial 3D models were obtained using our recently developed framework (PRIME) for *ab initio* single-particle 3D reconstruction (17). The standard technique used in biological single-particle cryo-EM (10) assigns each image the single best matching orientation, as determined by correlation matching to a gallery of reference images, obtained by projecting an *a priori* available 3D reference model. Two fundamental limitations of the standard technique are the bias introduced by the initial 3D model and the lack of mechanisms for modeling the alignment errors when data are noisy and the model is of poor quality. These limitations may be quite substantial when

reconstructing nanocrystals, because every particle is different and the particle population cannot be averaged, as in traditional single-particle EM. The individual frames also have a low SNR because of the relatively low per-frame electron dose and because of the granular background introduced by the liquid. PRIME overcomes these drawbacks by using weighted orientation assignment and stochastic optimization for determination of an optimal orientation weight distribution without any *a priori* information about the nanoparticles.

To initialize the 3D reconstruction process, we assigned the random orientations to images, producing a featureless spherical density map. The random orientations were refined by stochastic optimization of the correlation between the images and reprojections of the density map, using information from 30 Å to 3 Å and a discrete search space of orientations. The resulting initial model had a resolution of 2.5 Å according to the 0.143 Fourier shell correlation (FSC) criterion (21). We extended the PRIME algorithm by introducing a continuous orientation search space and used stochastic optimization to determine a continuous distribution of weights that related the continuous distribution of orientation parameters to the 3D reconstruction. Each round of the PRIME iterative alignment procedure involved determination of orientation weights for all particle images, followed by a weighted 3D reconstruction by direct Fourier reconstruction using a Kaiser-Bessel interpolation kernel. A few hundred iterations were executed, and in every round the FSC was calculated and used to construct a 3D Wiener filter that filtered the map such that the optimal SNR was obtained at the present resolution (22). The resolution of the final refined maps was measured to 2.10 Å (particle 1) and 2.14 Å (particle 2), respectively.

Even though the FSC methodology provides an accurate measure of the resolution when the reference structure used for matching has been appropriately low-pass filtered, it does not ensure against grossly incorrect structures. To validate our structures, we determined the agreement between the individual images used for reconstruction and the corresponding reprojections of the reconstructed 3D map. All image reprojection pairs (fig. S3) were generated for the two reconstructions, and the Fourier ring correlation (FRC) (23) was calculated between all pairs. The average FRC was larger than 0.143 to a resolution of 1 Å and showed a distinct peak spanning the 1 to 2 Å resolution region (fig. S3). This peak is due to the correlation between atomic densities in the reprojections and atomic densities in the images. We concluded that our reconstructions showed excellent agreement with the images. The spatial resolution is higher for particle 1, which has a larger number of frames, indicating that the present resolution can be improved by acquisition of longer movies that cover a wider range of rotational orientations.

We had anticipated that the Pt nanocrystals would have at least twofold rotational symmetry, perhaps even cubic symmetry. Remarkably, the

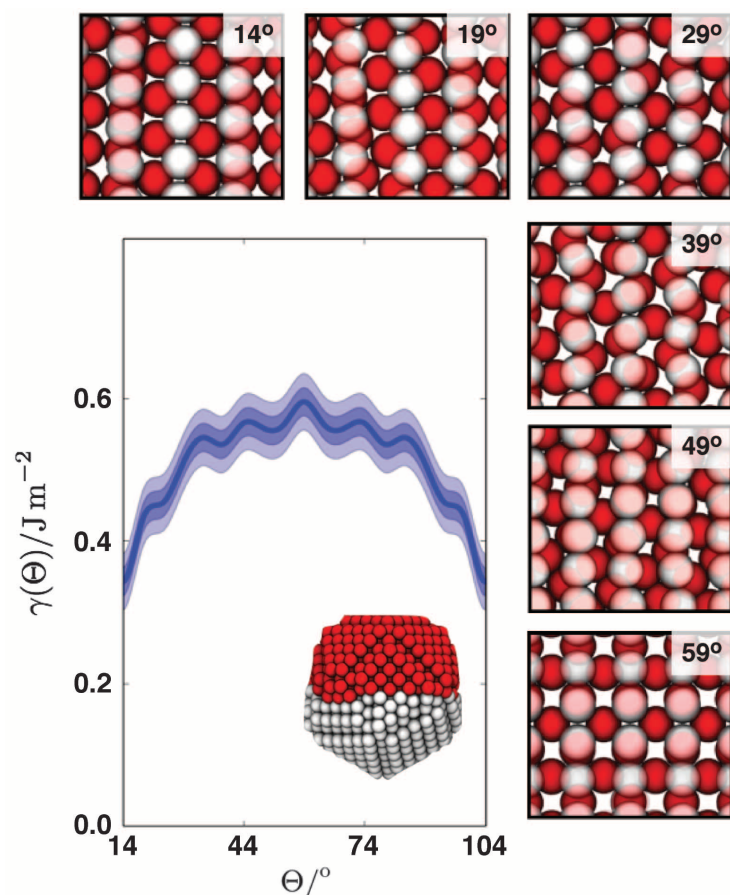


Fig. 4. Twist grain boundary free energies as a function of misalignment angle for the (110)-(100) crystal planes of a nanocrystal with 1135 atoms. Shaded regions indicate error bars of 1 and 2 standard deviations. The inset shows a relaxed nanocrystal with an initial misalignment angle of 14°. The non-flat grain boundary is located in the center of the nanocrystal. Images around the perimeter show the two relaxed planes at the grain boundary from the 100 (red) and 110 (white) grains for different misalignment angles.

reconstructions appeared asymmetrical, and attempts to apply C2, C4, C5, and D2 point-group symmetry by aligning the images to the principal symmetry axis and doing symmetric orientation refinement failed to improve the correlation between the reprojections and the images. This suggests that the Pt nanocrystals do not possess icosahedral, cubic, or pentagonal symmetry but are intrinsically asymmetrical. Reconstruction by the traditional single-particle cryo-EM technique, using an initial model based on a faceted face-centered cubic (fcc) nanoparticle, would suffer severe initial model bias and would not reproduce the true asymmetrical multidomain structure.

Our reconstructions of particles 1 and 2 revealed different asymmetrical crystal structures with the same underlying principle: a dense central disc of atomic planes (the core) with conical extensions anchored on each side, protruding in opposing and orthogonal directions with respect to the equatorial plane (see schematics in Fig. 2A with the lattice in different crystal domains colored blue and orange). Despite this similarity, the reconstructed 3D structures of the two Pt particles show interesting differences. First, the atomic arrangements on the surfaces observed in the EM density maps of particle 1 and 2 are distinct (Fig. 1C and Fig. 2E). Second, the two particles show different degrees of crystallinity in each domain. Whereas straight {111} crystal planes in three domains of particle 1 are shown throughout the cross-sectional images along the mid-vertical plane (Fig. 2B) and vertical planes at different depths (fig. S4), particle 2 shows more disordered internal structures within the domains. Also in particle 1, the conical protrusions have {111} atomic planes tilted with respect to the {111} atomic planes in the core. Particle 2 exhibits protrusions with a larger degree of disorder relative to the well-aligned {111} lattices in the particle 1 protrusions. Views of the reconstructions perpendicular to the equatorial plane (Fig. 2C) and a schematic illustration (Fig. 2D) show the overlaid lattices of the core (blue lines) and protrusions (yellow lines) with different tilting angles for particle 1 (14°) and particle 2 (7°).

The cross-sectional views along the equatorial plane (Fig. 2E) for particles 1 and 2 show similar arrangements of the {111} lattice planes, but cross-sectional images along the horizontal planes below and above the equatorial plane for the two particles (particle 1 in Fig. 3, C to E; particle 2 in fig. S5) indicate that the two particles are assembled by multiple domains but in unique geometries. The multiple domains and twisted grain boundaries that are present in the reconstructions are similar to previous observations of Pt nanocrystal growth trajectories, where small particles were observed to join along surfaces with low ligand coverage (3). The multidomain arrangement is also supported by other tomography reconstructions of larger Pt nanocrystals containing multiply twinned domains with decahedral symmetry and central screw dislocations (3, 5). Multidomain structures are common in many other colloidal metal nanoparticles, which likely evolve as a result of multiple coalescence events

during growth (3, 24–26). Our observation of heterogeneously structured Pt nanoparticles formed in the same solution confirms that individual particles from the same synthesis follow different nucleation and growth trajectories.

Figure 3A presents a 3D density map with colored sections indicating the upper (blue), core (gray), and lower (purple) domains of particle 1. Figure 3B shows a cross section perpendicular to the equatorial plane with the tentative atomic positions (different colored dots in each domain) indicating {111} lattice planes of fcc crystal that have repetition in every three crystal planes in all three crystal domains. Atoms closer to the surface seem to deviate farther from a perfect fcc structure. This is presumably explained by the fact that surface atoms are prone to relax excess free energy because of insufficient coordination and stabilization by surface ligand binding. In addition, the interface between the domains is disordered and not flat—a general consequence of the reduction in surface energies expected for nanoscale crystals relative to their bulk counterparts. The locations of three cross sections along horizontal planes (cross section 1, equator, and cross section 2) are indicated in Fig. 3A. Cross sections 1 and 2 are positioned near the interface between the central disk and the upper and lower conical protrusions, respectively. Cross section 1 exposes two facing surfaces from the upper and core domains (blue and gray densities in Fig. 3C, respectively). Cross section 1 shows a {100} surface with red dashed lines that trace the {111} planes exposed on the {100} surface. The cross section at the equator (Fig. 3D) exhibits a {110} surface, and blue dashed lines indicate the {111} planes exposed to the {110} surface. The red and blue lines are mapped onto the pseudo-atomic illustration of {100} and {110} surfaces with the proper orientation (a 14° rotation angle) in the right image of Fig. 3D. At cross section 2, near the interface between the central disk and the lower conical protrusion, a surface structure with pseudo {100} patterns traced by red dotted lines is exposed from the core and lower domains (gray and purple densities in Fig. 3E, respectively), which deviate from the ideal fcc structure. Figure 3 shows that the conical protrusions and the core join along {100} and {110} surfaces with distortions at the interface. Multiple domains merging along the low-index crystal planes, such as {100} and {110}, are presumably formed by coalescence events between small particles during the particle growth as a route to minimize excess surface energy. We previously observed a similar scenario: Two small Pt particles join along the {111} surfaces during growth (3). Presumably, coalescence along the low-index surfaces and the consequent evolution of the interface structure are mechanisms by which the nanocrystals reduce free energy.

To examine whether there is a thermodynamic rationale for the multidomain structures that we observed, we computed the free energies for the grain boundary formation and for the ligand-exposed surfaces. This was done using the Frenkel-Ladd method (27) for an embedded atom model of Pt (28), using an appropriate thermodynamics

integration path (fig. S6). We found that for low-angle misalignments, like those observed in particle 1 [14° rotation angle between {111} planes exposed on {110} and {100} surfaces from the central disk and upper domain in Fig. 3], the grain boundary free energy for a nanoparticle with 1200 atoms is 0.3 J/m², increasing to 0.55 J/m² for misalignment angles of up to 59° (Fig. 4). Small rotational relaxation of the crystal grains is found to be energetically viable at these interfaces, which may explain the orientation of the side protrusions in particle 1 with respect to its central section.

The surface free energy for the ligand-exposed interfaces was computed to be 2.8 J/m² as averaged over the {100} and {111} surfaces, weighted appropriately for the cuboctahedral shape. The disparity of scales between the grain boundary free energies and the much larger exposed surface free energies confirms that there is a large thermodynamic driving force for coalescence, even when such events result in grain boundary formation. As the free energy gain upon coalescence is much larger than thermal energies, initial aggregations are likely irreversible. The resultant grain boundaries are then kinetically arrested over laboratory time scales (see supplementary materials).

Our results show that the SINGLE methodology can be used to investigate the structural principles underlying the assembly and transient morphology of any stable, small nanoparticle in solution. We envision that SINGLE can be applied directly to in situ 3D structural studies of many other kinds of solvated particles.

REFERENCES AND NOTES

1. D. Mocatta *et al.*, *Science* **332**, 77–81 (2011).
2. H. Zhang, T. Watanabe, M. Okumura, M. Haruta, N. Toshima, *Nat. Mater.* **11**, 49–52 (2012).
3. J. M. Yuk *et al.*, *Science* **336**, 61–64 (2012).
4. H. Zheng *et al.*, *Science* **324**, 1309–1312 (2009).
5. C.-C. Chen *et al.*, *Nature* **496**, 74–77 (2013).
6. P. A. Midgley, R. E. Dunin-Borkowski, *Nat. Mater.* **8**, 271–280 (2009).
7. P. A. Midgley, M. Weyland, *Ultramicroscopy* **96**, 413–431 (2003).
8. C. Zhu *et al.*, *Phys. Rev. B* **88**, 100201 (2013).
9. S. Van Aert, K. J. Batenburg, M. D. Rossell, R. Erni, G. Van Tendeloo, *Nature* **470**, 374–377 (2011).
10. Y. Cheng, T. Walz, *Annu. Rev. Biochem.* **78**, 723–742 (2009).
11. H. Elmlund, D. Elmlund, S. Bengio, *Structure* **21**, 1299–1306 (2013).
12. K. Murakami *et al.*, *Science* **342**, 1238724 (2013).
13. M. Azubel *et al.*, *Science* **345**, 909–912 (2014).
14. B. Goris *et al.*, *Nat. Mater.* **11**, 930–935 (2012).
15. M. C. Scott *et al.*, *Nature* **483**, 444–447 (2012).
16. A. Leis, B. Rockel, L. Andrees, W. Baumeister, *Trends Biochem. Sci.* **34**, 60–70 (2009).
17. C. V. Robinson, A. Sali, W. Baumeister, *Nature* **450**, 973–982 (2007).
18. M. Battaglia *et al.*, *Nucl. Instrum. Methods Phys. Res. A* **598**, 642–649 (2009).
19. Q. Chen *et al.*, *Nano Lett.* **13**, 4556–4561 (2013).
20. R. N. Bracewell, *Aust. J. Phys.* **9**, 198–217 (1956).
21. M. van Heel, M. Schatz, *J. Struct. Biol.* **151**, 250–262 (2005).
22. P. B. Rosenthal, R. Henderson, *J. Mol. Biol.* **333**, 721–745 (2003).
23. W. O. Saxton, W. Baumeister, *J. Microsc.* **127**, 127–138 (1982).
24. M. Takesue *et al.*, *J. Am. Chem. Soc.* **133**, 14164–14167 (2011).
25. J. Polte *et al.*, *ACS Nano* **6**, 5791–5802 (2012).
26. J. Polte *et al.*, *ACS Nano* **4**, 1076–1082 (2010).
27. D. Frenkel, A. J. C. Ladd, *J. Chem. Phys.* **81**, 3188–3193 (1984).
28. H. W. Sheng, M. J. Kramer, A. Cadien, T. Fujita, M. W. Chen, *Phys. Rev. B* **83**, 134118 (2011).

ACKNOWLEDGMENTS

Supported by the Physical Chemistry of Inorganic Nanostructures Program (KC3103), Office of Science, Office of Basic Energy Sciences, U.S. Department of Energy (DOE) under contract

DE-AC02-05CH11231 (J.P. and A.P.A.); NSF grant DMR-1310266, Harvard Materials Research Science and Engineering Center grant DMR-1420570, and Amore Pacific (J.P., S.H.H., and D.A.W.); the Multimodal Australian Sciences Imaging and Visualization Environment (www.massive.org.au) and funds from Monash University (H.E.); the DOE Office of Energy Research, Basic Energy Sciences, Materials Sciences and Engineering Division under contract DE-AC02-05CH11231 within the SP2-Bonded Materials Program and the Molecular Foundry (construction of GLC and TEM characterization), Office of Naval Research grant

NO0014-12-1 (graphene growth), NSF grant DMR-1206512 (graphene transfer methods development), and postdoctoral support from Defense Threat Reduction Agency grant HDTRA1-13-1-0035 (J.M.Y., K.K., and A.Z.); the Princeton Center for Theoretical Science (D.T.L.); a Miller fellowship from Miller Institute for Basic Research in Science at UC Berkeley (Q.C.); and the Basic Science Research Program through the National Research Foundation of Korea funded by Ministry of Education grant NRF-2014R1A1A2058178 (K.K.). Electron microscopy was performed at the Molecular Foundry supported by DOE contract DE-AC02-05CH11231.

SUPPLEMENTARY MATERIALS

www.sciencemag.org/content/349/6245/290/suppl/DC1
Molecular Dynamics Simulation
Materials and Methods
Figs. S1 to S9
References (29–38)
Movies S1 to S4

16 March 2015; accepted 4 June 2015
10.1126/science.aab1343

ANIMAL PHYSIOLOGY

Summer declines in activity and body temperature offer polar bears limited energy savings

J. P. Whiteman,^{1,2*} H. J. Harlow,² G. M. Durner,³ R. Anderson-Sprecher,⁴ S. E. Albeke,⁵ E. V. Regehr,⁶ S. C. Amstrup,⁷ M. Ben-David^{1,2}

Polar bears (*Ursus maritimus*) summer on the sea ice or, where it melts, on shore. Although the physiology of “ice” bears in summer is unknown, “shore” bears purportedly minimize energy losses by entering a hibernation-like state when deprived of food. Such a strategy could partially compensate for the loss of on-ice foraging opportunities caused by climate change. However, here we report gradual, moderate declines in activity and body temperature of both shore and ice bears in summer, resembling energy expenditures typical of fasting, nonhibernating mammals. Also, we found that to avoid unsustainable heat loss while swimming, bears employed unusual heterothermy of the body core. Thus, although well adapted to seasonal ice melt, polar bears appear susceptible to deleterious declines in body condition during the lengthening period of summer food deprivation.

The current rate of Arctic sea-ice loss, unprecedented in at least the past several thousand years, is outpacing predictions and accelerating (1). This raises concerns about the persistence of polar bears (*Ursus maritimus*) (2), which hunt on the surface of the sea ice, most successfully between April and July (3), when ringed seals (*Pusa hispida*) use this substrate for rearing pups and molting (4). Between August and October, hunting can be poor (5) as seals reduce ice surface time (4). Additionally, in about two-thirds of the polar bear range (6), seals become largely pelagic as ice retreats from the continental shelf (7, 8). Some polar bears spend this period on shore, where foraging is also usually limited (9).

To reduce the loss of body condition during summer food deprivation, shore bears purportedly enter a state of lowered activity and resting metabolic rate similar to winter hibernation but without denning (10). This “walking hibernation” could partially compensate for the nega-

tive impacts of extended ice melt (11). However, in western Hudson Bay, Canada, shore bears lose body mass at a rate indicative of typical, rather

than hibernation-like, metabolism (12). The physiological state of bears that follow the retreating sea ice into the central Arctic basin in summer is unknown. In addition, recent sea-ice loss may be increasing the frequency of long-distance swims by polar bears (13), during which they risk losing over 10 times more heat than they produce (supplementary text) because their fur loses 90% of its insulation value when wet (14), and their subcutaneous fat does not provide blubber-like insulation (15).

To understand polar bear responses to these challenges of summer ice melt, we investigated activity on shore (2008 and 2009) and on ice (2009) in the Beaufort Sea (Fig. 1) by affixing telemetry transmitters and activity loggers (16) to 25 females (mean age = 10 years \pm 1 SE, age range = 4 to 20 years) and one male (age 3). We recorded temperatures of the body core (an index of metabolic rate) (17) and periphery by implanting loggers into the abdomens (core) of 10 bears (nine females, mean age = 11 years \pm 2 SE, age range = 3 to 23 years; one male, age 6) and the rumps (periphery) of seven other individuals (six females, mean age = 9 years \pm 2 SE, age range = 5 to 20 years; one male, age 2).

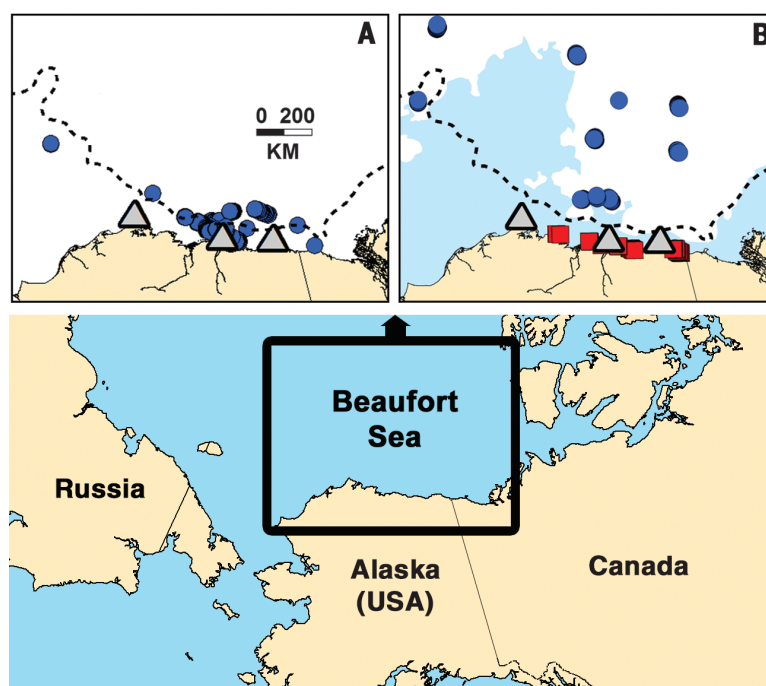


Fig. 1. The western Arctic on (A) 11 May 2009 and (B) 31 August 2009. Locations are shown for ice polar bears (blue circles), shore polar bears (red squares), and whale carcasses (triangles). The 300-m depth contour is shown as a dashed line. Sea ice is shown in white.

¹Program in Ecology, University of Wyoming, Laramie, WY 82071, USA. ²Department of Zoology and Physiology, University of Wyoming, Laramie, WY 82071, USA. ³U.S. Geological Survey, Alaska Science Center, Anchorage, AK 99508, USA. ⁴Department of Statistics, University of Wyoming, Laramie, WY 82071, USA. ⁵Wyoming Geographic Information Science Center, University of Wyoming, Laramie, WY 82071, USA. ⁶Marine Mammals Management, U.S. Fish and Wildlife Service, Anchorage, AK 99503, USA. ⁷Polar Bears International, Bozeman, MT 59772, USA.

*Corresponding author. E-mail: jwhitema@uwyo.edu

This copy is for your personal, non-commercial use only.

If you wish to distribute this article to others, you can order high-quality copies for your colleagues, clients, or customers by [clicking here](#).

Permission to republish or repurpose articles or portions of articles can be obtained by following the guidelines [here](#).

The following resources related to this article are available online at www.sciencemag.org (this information is current as of July 16, 2015):

Updated information and services, including high-resolution figures, can be found in the online version of this article at:

<http://www.sciencemag.org/content/349/6245/290.full.html>

Supporting Online Material can be found at:

<http://www.sciencemag.org/content/suppl/2015/07/15/349.6245.290.DC1.html>

A list of selected additional articles on the Science Web sites **related to this article** can be found at:

<http://www.sciencemag.org/content/349/6245/290.full.html#related>

This article **cites 38 articles**, 6 of which can be accessed free:

<http://www.sciencemag.org/content/349/6245/290.full.html#ref-list-1>

This article has been **cited by** 1 articles hosted by HighWire Press; see:

<http://www.sciencemag.org/content/349/6245/290.full.html#related-urls>

This article appears in the following **subject collections**:

Materials Science

http://www.sciencemag.org/cgi/collection/mat_sci